Engineering Applications of Computational Fluid Mechanics Vol. 7, No. 4, pp. 533-543 (2013)

CFD ANALYSES OF SYNGAS-FIRED INDUSTRIAL TILES KILN MODULE

Marco Cavazzuti*[+], Mauro A. Corticelli*, Gianluca Masina[#] and Roberto Saponelli[^]

** Dipartimento di Ingegneria "Enzo Ferrari", Università degli Studi di Modena e Reggio Emilia, via Vignolese 905, 41125 Modena, Italy*
[#] Sacmi Forni S.p.A., via dell'Artigianato 10, 40123, Salvaterra di Casalgrande, Italy
[^] Sacmi S.C., via Selice Provinciale 17/A, 40026, Imola, Italy
[+] Email: marco.cavazzuti@unimore.it (Corresponding Author)

ABSTRACT: Industrial kilns for ceramic tiles production demand thorough control of the firing parameters to ensure uniform product quality. A given temperature profile must be imposed along the kiln length, while spanwise temperature profile should be as uniform as possible at the tiles level at any location. Due to special needs in emerging markets, interest is growing towards the use of gases produced by gasification processes as an alternative to methane. This requires specific burner design and proper re-calibration of the firing parameters. In the present work, computational fluid dynamics is used to analyse an industrial kiln section for different fuels, nominal burner powers, and burner nozzle diameters. The results are given in terms of temperature and velocity fields in the kiln room, and temperature distributions over the tiles floor. It is shown that a sensible combination of the three parameters investigated can lead to satisfactory results, even with gases having poor heating value.

Keywords: industrial kiln, syngas, CFD analysis

1. INTRODUCTION

In industrial ceramic production, tiles are usually fired using continuous roller methane gas kilns. These kilns are long up to a few hundred meters, and up to a thousand burners are placed along the kiln length both above and below the tiles level. The tiles moving on rollers along the kiln undergo a given temperature history since the different sections of the kiln are differently heated. At the end of the firing process warm impinging air jets cool down the hot tiles before reaching the kiln exit. The exhaust gases from the burners are expelled directly into the kiln room, and are usually sucked by a unique intake manifold located upstream by the kiln entrance. A general scheme of a kiln section is shown in Fig. 1.

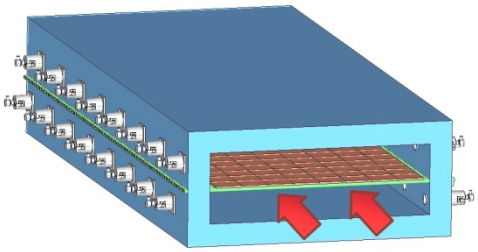

Fig. 1 Scheme of a kiln section including kiln walls (made of refractory materials), burners, rollers, and tiles. The tiles move on rollers in the lengthwise direction (as shown by the arrows) while the exhaust gases are sucked in the opposite direction.

Important factors for a correct firing, so as to guarantee a good product quality, are the kiln lengthwise and spanwise temperature profiles. The former is responsible for the tiles temperature history that must be able to catalyse different reactions at different times during firing. The latter needs to be as uniform as possible so that all the tiles are subject to the same temperature history regardless of their spanwise locations within the kiln, thus ensuring the product uniformity.

In emerging markets it is of interest to substitute synthesis gases for methane. Of course, such a choice impacts on the kiln fluid dynamic behaviour and calls for a specific fuel-dependent burner design. Also, the kiln firing parameters must be re-calibrated since the final product quality and uniformity would definitely deviate from expectations from methane-based experiments.

The use of Computational Fluid Dynamics (CFD) has been demonstrated to constitute a viable alternative to experimental analyses in several industrial applications, since reductions in cost and time-to-market can rapidly be achieved. However, to the author's knowledge, no CFD exercise available in the literature is devoted to roller-kilns for tiles production and the prediction

Received: 7 May 2013; Revised:1 Aug. 2013; Accepted: 2 Sep. 2013

of their performance under different operating conditions.

A few CFD analyses of kilns have been presented, particularly in recent years, mainly focusing on food processing. For instance, in Mirade et al. (2004) and Wong et al. (2006) kilns for biscuits and bread baking were considered, respectively. In dealing with bread baking other papers also presented the development of models for assessing bread quality (Therdthai et al., 2004) and transient heat transfer in a bakery oven (Boulet et al., 2010). Williamson and Wilson (2009) discussed the importance of radiant heat transfer and air moisture content in the final product quality, and numerically investigated a radiant burner for food baking processes. A different application is found in Smolka et al. (2010) where the performance of a laboratory dry oven was assessed by means of 3D CFD simulations.

For large industrial kilns quite some attention has been devoted to rotary kilns for cement production. Several aspects of the industrial process were addressed, earlier work being more oriented to a comprehensive CFD modelling of the various phenomena occurring in the kilns (Mastorakos et al., 1999), while recent works were more devoted to efficiency improvement in terms of emissions (Mikulčić et al., 2012) or heat recovery (Söğüt et al., 2010).

Continuous roller kilns for tiles production are quite different from ovens for food processing, at least for what concerns size, temperature regimes, and thermal powers at play (up to 300 m length, 1250 °C, and 15 MW, respectively). On the other hand, rotary kilns are much different in the way they work due to the facts that the heated material is continuously mixed inside the kiln, and that most of the heat is absorbed by the strongly endothermic reaction that takes place in the formation of calcium oxide from calcium carbonate.

In this paper, 3D CFD analyses of an industrial kiln module for tiles production are performed for two different synthesis fuels (referred to in the following as syngas #1 and syngas #2) and for methane. Two nominal burner powers (38.0 kW and 12.7 kW), and two burner nozzle diameters (50 mm and 40 mm) are considered for each fuel. Simulations with methane are used for the sake of comparison to syngases. Only a section of the kiln is taken into consideration since it would require a huge amount of computational resources for the kiln to be addressed as a whole. Although a small modular section may not be fully representative of the behaviour of a real kiln, this allows us to investigate several parameters and to quantify the impact they may have on the temperature distribution in the module.

Temperature and velocity fields within the module, and temperature distributions over the tiles floor are presented and discussed. The latter parameter is particularly meaningful since in industrial kilns for ceramic tiles the temperature uniformity over the product surface is directly related to the final product quality. A uniform product quality is indeed the main challenge to be addressed, especially when the call for higher productivity and reduced overall dimensions pushes the design toward the adoption of larger spanwise dimensions.

2. PROBLEM DEFINITION

2.1 Numerical domain and mesh

The dimensions of the kiln module considered in the present study (Fig. 2(a)) are 3650×525×566 mm, where the larger dimension corresponds to the spanwise size of a real kiln. These follow from a similar device used by Sacmi Forni S.p.A. for experimental analyses. A single burner is installed on one of the smaller side walls; the location of the burner outlet/kiln module inlet section is pointed out by an arrow in Fig. 2. On the opposite side (not visible in Fig. 2), a small gap (45×525 mm wide) located in the upper part of the wall serves as the exhaust gas outlet.

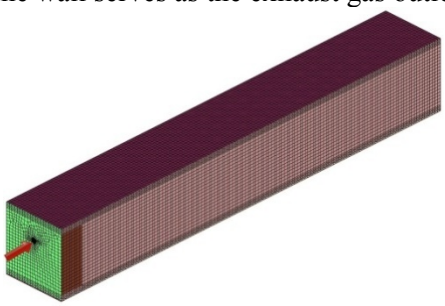

(a) Kiln module used for 12.7 kW cases

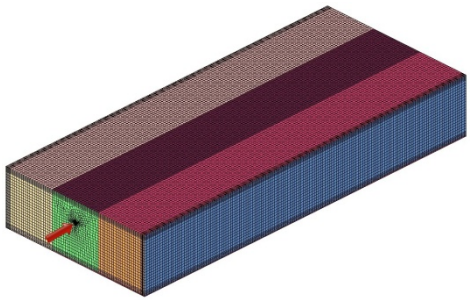

(b) Kiln module used for 38.0 kW cases

Fig. 2 Kiln modulus geometries. The arrows indicate the locations of the burner outlet serving as mass flow inlet in the present study.

Such a domain is employed for low nominal burner power simulations (12.7 kW). High burner power simulations are carried out for a three-fold nominal power (38.0 kW) on the three-fold volume domain shown in Fig. 2b, whose dimensions are 3650×1575×566 mm.
This larger domain was meshed for CFD purposes with 370 thousand elements while the smaller domain with 120 thousand. The mesh is hexahedral except for the area neighbouring the hot gases inlet section where a few layers of tetrahedral elements link the finer triangular mesh of the nozzle surface to the rest of the domain.
The burner geometry had been dealt with by the authors in a previous study (Cavazzuti *et al.*, 2013) and is not included in the present simulations. The information gained from previous analyses is exploited here.
Finer meshes having 1 and 3 million elements for the smaller and the larger domains respectively were tested too. The differences in terms of average quantities such as floor temperature, or thermal dissipation at the walls is negligible (*e.g.* lower than 0.2 % for the temperature and lower than 0.1 % for the thermal dissipation). Larger yet small differences are found when comparing local quantities. In fact, with a finer mesh the hot jet coming from the burner nozzle is more compact and slightly less penetrating due to smaller numerical diffusion as shown in Fig. 3. The difference is more evident for 38.0 kW cases. From these considerations the finer mesh was adopted for the current study since it was considered to give sufficiently accurate results. Unfortunately, for this particular setup, no experimental data was available for a more proper model validation. In any case, in the following it will be shown how the temperatures at play in the numerical model are comparable to those commonly found in real kilns.

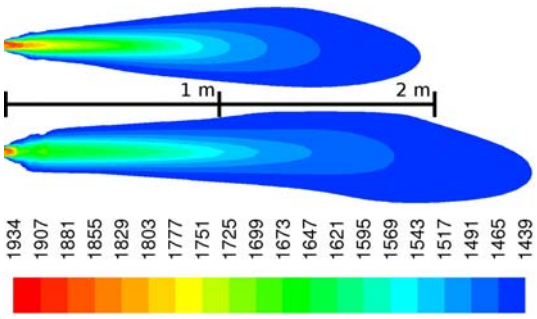

Fig. 3 Temperature contours on vertical plane for hot gas jet entering kiln room for syngas #1, $D = 40$ mm, $\dot{Q}_n = 38.0$ kW case; 3 million elements mesh (top) versus 370 thousand elements mesh (bottom).

2.2 CFD setup and fuel gas properties

Simulations were performed using the commercial CFD code Fluent 6.3. A steady-state pressure-based implicit solver with first-order upwind discretization and SIMPLE pressure-velocity coupling was chosen. A Discrete Ordinates (DO) radiation model was adopted, together with a k-ε realizable turbulence model with enhanced wall functions.
The choice of enhanced wall functions against standard wall functions was due to the fact that typical average y^+ values, in the simulations performed, ranged between 3.0 and 5.5. First-order discretization schemes were chosen after second-order schemes were also tested and resulted in unremarkable differences between the simulation runs.
Concerning the combustion model an equilibrium, non-adiabatic, non-premixed combustion model was used. With this model the combustion is simplified to a mixing problem where two transport equations are solved, one for the mean mixture fraction f_m and one for the mean mixture fraction variance f_v, in place of individual species transport for each chemical component at play. These are:

$$\frac{\partial(\rho f_m)}{\partial t} + \nabla \cdot (\rho \boldsymbol{v} f_m) = \nabla \cdot \left(\frac{\mu_t}{\sigma_t} \nabla f_m\right) \quad (1)$$

$$\frac{\partial(\rho f_v)}{\partial t} + \nabla \cdot (\rho \boldsymbol{v} f_v) = \nabla \cdot \left(\frac{\mu_t}{\sigma_t} \nabla f_v\right) + C_g \mu_t (\nabla f_m)^2 - C_d \rho \frac{\varepsilon}{k} f_v \quad (2)$$

where f_m and f_v are Favre averaged quantities, ρ is fluid density, $\boldsymbol{v}$ is velocity, μ_t is turbulent dynamic viscosity, and k and ε are the turbulent kinetic energy and dissipation rate, respectively. C_g, C_d, and σ_t are constants with values 2.86, 2.00, and 0.85, respectively.
Components concentrations are derived from mixture fraction distribution by use of a pre-processed look-up table. Turbulence effects are included through a probability density function of the mixture fraction fluctuations. The combustion model is rather simple and computationally efficient since no chemical kinetics is computed explicitly, and is most suitable for turbulent diffusion flames with fast chemical kinetics.
Thermal Boundary conditions (BCs) are set as follows. The left and the right walls (looking at the kiln module from the burner side) are adiabatic, on the remaining walls (floor, ceiling, burner side and outlet side walls) the physical

Table 1 Physical parameters and boundary conditions at kiln walls.

Walls	Floor & ceiling	Burner & outlet
Thickness (mm)	315	355
External heat transfer coefficient (W/m^{2}K)	12	12
External temperature (K)	298	298
Internal emissivity	0.9	0.9
External emissivity	0.9	0.9
Thermal conductivity (W/mK)	0.380	0.185

parameters and applied boundary conditions are listed in Table 1. The same conditions are adopted on opposite walls for simplicity, even though in real kilns different situations may be found in general. The values for thickness, conductivity and emissivity are representative of walls of a real kiln. The external temperature and heat transfer coefficient instead are guessed on the basis of typical ambient conditions that can be found in the large warehouse of a tiles production plant. The BCs at the wall allow to model the effects of conduction, convection, and radiation in the kiln, so as to estimate thermal loss across the walls.

For the rest, no-slip conditions are imposed at the walls, and for the turbulent quantities the BCs follow from the wall functions formulation adopted.

As already mentioned, the exhaust gas outlet in a real kiln would generally be located upstream by the tiles entrance section. As the current analysis is limited to a section of the kiln, a different outlet section must be provided for the numerical domain. This has been chosen to be the furthest from the nozzle and the tiles floor (that is, in the upper part of the rear wall) in order to limit its influence on the temperature profile in the kiln section, and in particular on the tiles floor. Even though such a configuration for the kiln outlet section is not customary, in any case it is of interest since lately kiln producers are questioning themselves on whether a distributed exhaust collector system may be more profitable, compared to the traditional unique intake manifold, in view of a more efficient *in situ* exploitation of the heat recovery systems.

The velocity profile and the flow characteristics (*e.g.* temperature, turbulence kinetic energy and dissipation rate, mean mixture fraction and variance) at the burner outlet nozzle are taken from the preliminary simulations of the whole burner and are imposed as inlet BCs on the kiln side in the present study.

Typical inlet profiles are shown in Fig. 4 for one of the cases, together with CO and CO_2 mass fraction contours. The last two profiles are not imposed directly into the simulation in that they follow from the look-up table depending on the values of f_m and f_v. They are reported here to show that the combustion process is not fully completed inside the burner, and some unburnt fuel is still present at the burner outlet section (Fig. 4e). This implies that the modelling of combustion must necessarily be embodied in the present simulations. The small asymmetries in the contours of Fig. 4 are due to the non-fully symmetrical fluid flow generated inside the burner causing the flame to be slightly tilted upward due to internal geometrical asymmetries.

The air and fuel gas mass flow rates in the burner simulations were chosen so that the burner nominal power $\dot{Q}_n$ was matched with a 10 % air excess over the stoichiometric ratio. This translates into

$$\dot{M}_f = \frac{\dot{Q}_n}{LHV} \tag{3}$$

$$\dot{M}_a = 1.1\, AFR_{st} \dot{M}_f \tag{4}$$

where $\dot{M}_f$ and $\dot{M}_a$ are mass flow rates for the fuel and the combustive agent (air), respectively, LHV is the fuel Lower Heating Value, and AFR_{st} the stoichiometric air-to-fuel ratio.

The chemical composition and the properties of the fuel gases used are summarized in Table 2.

The actual behaviour of the solid tiles floor is difficult to model since it changes continuously during firing and depends on a number of parameters. The tiles react in different ways mainly depending on temperature, temperature history, and chemical composition. The temperature history, in fact, should be able to catalyse different reactions at given times, and both endothermic and exothermic reactions are found during firing. Moreover, different types of tiles, in terms of chemical composition, require different temperature histories and different sequences of reactions to occur, also, releasing different gaseous compounds into the kiln room environment at different stages. Thus, it is not possible to define a general interaction of the tiles with the environment of the kiln that would hold under any circumstance.

For these reasons, in the present study the presence of the tiles is modelled as a passive inert 5 mm thick solid layer on the top of the kiln section floor. This means the tiles layer, in

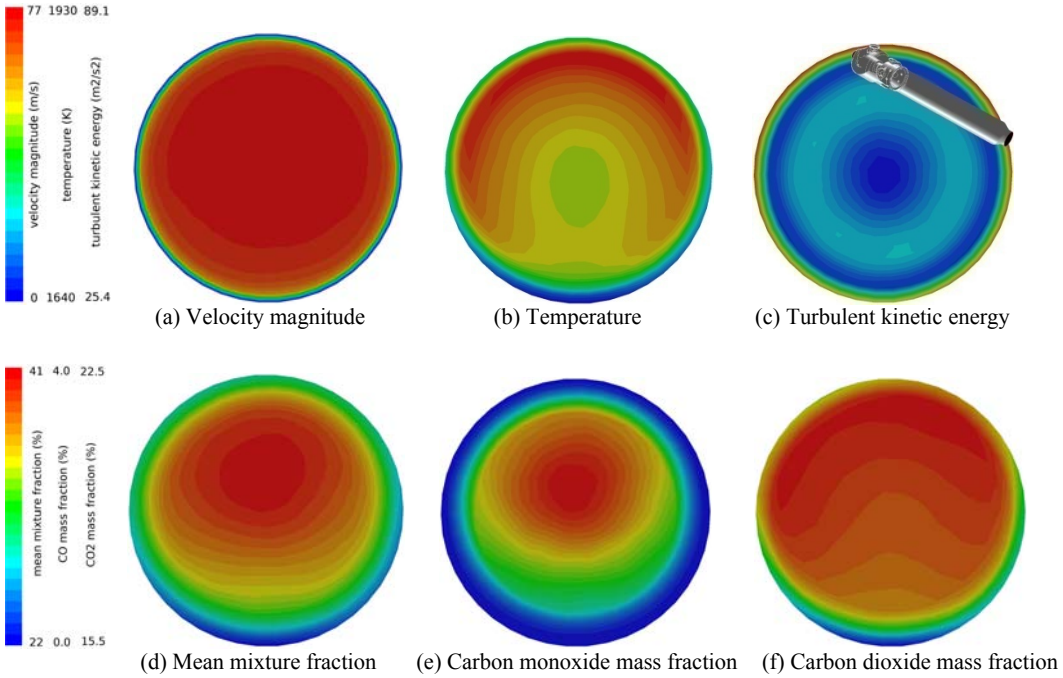

(a) Velocity magnitude (b) Temperature (c) Turbulent kinetic energy

(d) Mean mixture fraction (e) Carbon monoxide mass fraction (f) Carbon dioxide mass fraction

Fig. 4 Contour fields on burner nozzle section after burner simulations in Cavazzuti *et al.* (2013). The figures refer to syngas #1, $D = 40$ mm, $\dot{Q}_n = 38.0$ kW case. A scheme of the burner geometry where the outlet section is highlighted is reported on the top right end of the figure.

Table 2 Fuel gas and combustive agent mass fraction chemical composition and properties.

Chemical specie	Syngas #1	Syngas #2	Methane	Dry air
H_2	0.014	0.009	–	–
CH_4	0.014	0.022	1.000	–
CO	0.389	0.136	–	–
CO_2	0.047	0.278	–	–
O_2	0.003	–	–	0.231
N_2	0.479	0.450	–	0.756
H_2O	0.054	0.105	–	–
Ar	–	–	–	0.013
$\boldsymbol{AFR_{st}}$	1.653	1.009	17.235	–
LHV (MJ/kg)	6.26	3.51	50.01	–

practice, only serves as an additional thermal resistance term on the lower wall having little influence on the overall floor temperature distribution.

Concerning the fluid thermal properties, the specific heat of the air/fuel gas mixture is computed through the mixing law starting from JANAF coefficients for every chemical component. The mixture thermal conductivity varies linearly with the temperature, while the dynamic viscosity follows the Sutherland law

$$\mu = \mu_0 \frac{T_0 + S}{T + S} \left(\frac{T}{T_0} \right)^{\frac{3}{2}} \tag{5}$$

where μ is the mixture viscosity, T is the temperature, and μ_0, T_0 and S are constants, namely: $\mu_0 = 1.716 \times 10^{-5}$ Pa s, $T_0 = 273.11$ K and $S = 110.56$ K.

2.3 Simulated operating conditions

As premised, three different fuel gases were tested (syngas #1, syngas #2, and methane), for two different diameters D of the burner nozzle (40 mm and 50 mm), and for two typical burner nominal powers encountered in industrial kilns $\dot{Q}_n$ (12.7 kW and 38.0 kW), resulting in twelve case studies overall. Due to the problem size, the

numerical model shows a very large inertia. In fact, with a kiln module volume between 1.8 and 3.25 m^3, and mass flow rates at the inlet between 5 and 23 g/s, a few hundred thousand iterations were required before reaching convergence. As a consequence, the simulations were particularly time-consuming requiring two to four weeks of CPU time each when running on a single processor.

3. RESULTS

3.1 Temperature and velocity distributions

The results of the simulations are shown in Table 3 in terms of average temperature on the tiles floor (T_{fl}) and in the room (T_{rm}), and maximum temperature difference between the hottest and the coldest spots on the tiles floor (ΔT_{fl}).

It must be noted that the values of ΔT_{fl} for cases with $\dot{Q}_n = 12.7$ kW are negatively affected by the low velocity of the mixture at the burner nozzle and within the domain. This prevents the hot gas from reaching the end of the kiln room before being cooled down. This is shown in Figs. 5 and 6 where the velocity distribution on the axial vertical plane and the temperature distribution on the tiles floor are shown for both low and for high $\dot{Q}_n$ values.

It is pointed out that temperature data at the tiles floor are not representative of the effective floor temperature distribution in a real kiln, where the burners are placed alternately on the lateral walls (as shown in Fig. 1). In this way, the cold end in Fig. 6a would actually be warmed up by the two nearer burners on the opposite wall.

These first considerations suggest that the mixture velocity is likely to play an important role on the temperature distribution over the tiles floor. Even though this is a rather obvious conclusion, since higher velocity means more mixing and stronger convection, it is not necessarily true that the fastest the fluid the better.

In fact, Table 3 shows that for each fuel type, in view of ΔT_{fl} minimization, 40 mm nozzles constantly overperform 50 mm ones, and 38.0 kW cases overperform 12.7 kW ones. However, from the energy saving point of view, looking at the temperatures that are achieved in the room and on the tiles floor, the opposite is true.

Considering that high $\dot{Q}_n$ cases are run for a three-fold power on a three-fold volume with a three-fold surface area through which heat is lost, the various cases are quite similar to each other. Under the assumption of complete combustion, which is always attained here, two factors are mainly responsible for the differences in T_{fl} and T_{rm} between the cases in Table 3:

- the fluid velocity: faster fluids mix faster, but less efficiently due to their lower residence time, and leave the kiln room at higher temperatures compared to the kiln average,
- the total fluid mass flow rate ($\dot{M}_t = \dot{M}_f + \dot{M}_a$): for continuity reasons, under steady-state operating conditions the higher the mass flow rate, the higher the net power leaving the kiln room in the form of sensible enthalpy.

Even though these two factors are obviously quite closely correlated, the former is responsible for the temperature differences among cases having the same fuel and the same $\dot{Q}_n$ ($\Delta T \approx 17$ °C on average, according to Table 3). The latter is responsible for the temperature differences among cases having the same fuel and the same nozzle diameter ($\Delta T \approx 52$ °C on average, according to Table 3).

Fig. 7 confirms the influence of the fluid velocity by showing the pathlines from the burner nozzle for two cases having high (Fig. 7a) and low (Fig. 7b) velocities at the nozzle. While in the latter case the jet quickly loses velocity and is barely able to reach half the length of the kiln module before being caught up in big vortices; in the former the jet reaches the outlet area on the far-end of the room in less than 1 s.

Fig. 8 compares the axial vertical plane temperature distributions for two low power cases. Where the nozzle diameter is larger (Fig. 8b) temperature diffusion is more evident. This brings along a larger average temperature as demonstrated by the contour lines. At the same time the temperature distribution on the tiles floor is less uniform, as shown in Table 3.

A clearer quantitative insight into the floor temperature distribution for the twelve simulations performed is given in Fig. 9 where the temperature trend along the burner axis projection on the tiles floor is shown. For a better and easier comparison of the trends, the temperatures in the plot have been transposed so that the zero level corresponds to the floor temperature by the burner nozzle, whatever its value.

On average, high $\dot{Q}_n$ cases show a four to eight times lower temperature difference on the tiles floor. This is in favour of the initial idea that larger mass flow rates and velocities promote the floor temperature uniformity. In particular, it is

Table 3 Kiln module floor and room average temperatures.

Case study	T_{fl} (K)	ΔT_{fl} (K)	T_{rm} (K)
Syngas #1, $\dot{Q}_n = 12.7$ kW, $D = 40$ mm	1492.5	37.8	1497.9
Syngas #1, $\dot{Q}_n = 12.7$ kW, $D = 50$ mm	1533.4	44.1	1538.4
Syngas #1, $\dot{Q}_n = 38.0$ kW, $D = 40$ mm	1417.4	6.2	1423.2
Syngas #1, $\dot{Q}_n = 38.0$ kW, $D = 50$ mm	1430.1	9.1	1435.8
Syngas #2, $\dot{Q}_n = 12.7$ kW, $D = 40$ mm	1246.8	34.2	1253.1
Syngas #2, $\dot{Q}_n = 12.7$ kW, $D = 50$ mm	1263.4	43.6	1269.5
Syngas #2, $\dot{Q}_n = 38.0$ kW, $D = 40$ mm	1210.2	10.2	1216.5
Syngas #2, $\dot{Q}_n = 38.0$ kW, $D = 50$ mm	1215.5	10.2	1221.8
Methane, $\dot{Q}_n = 12.7$ kW, $D = 40$ mm	1485.7	40.6	1491.4
Methane, $\dot{Q}_n = 12.7$ kW, $D = 50$ mm	1504.7	46.2	1510.2
Methane, $\dot{Q}_n = 38.0$ kW, $D = 40$ mm	1464.5	7.2	1470.1
Methane, $\dot{Q}_n = 38.0$ kW, $D = 50$ mm	1472.1	11.9	1477.7

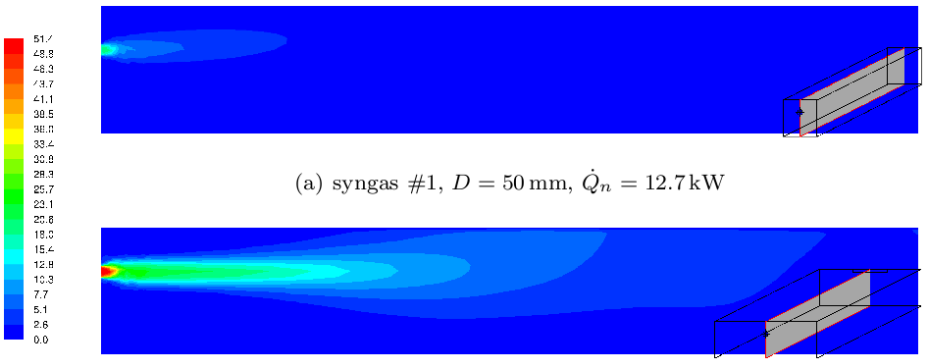

(a) syngas #1, $D = 50$ mm, $\dot{Q}_n = 12.7$ kW

(b) syngas #1, $D = 50$ mm, $\dot{Q}_n = 38.0$ kW

Fig. 5 Velocity field along kiln axial vertical plane (unit: m/s). Axial vertical plane refers to the vertical plane passing through the burner nozzle axis as shown in the outlines at the right end of the figures.

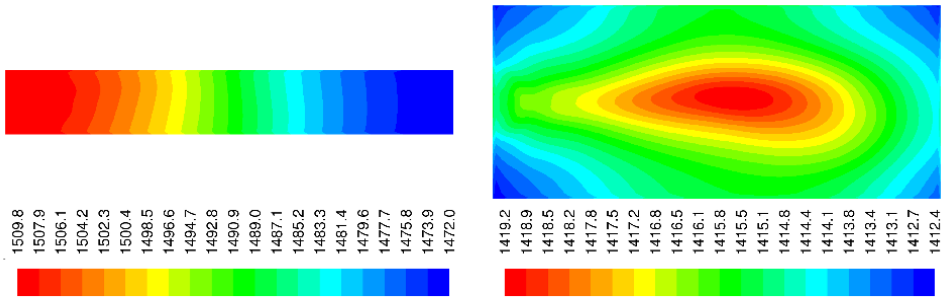

(a) syngas #1, $D = 40$ mm, $\dot{Q}_n = 12.7$ kW (b) syngas #1, $D = 40$ mm, $\dot{Q}_n = 38.0$ kW

Fig. 6 Temperature field on tiles floor (unit: K).

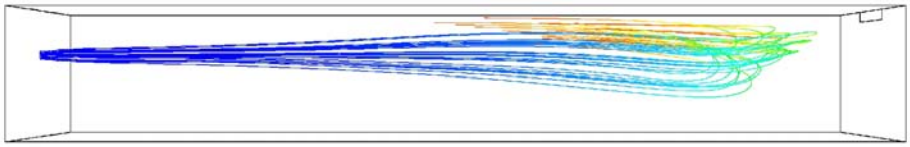

(a): syngas #2, $D = 40$ mm, $\dot{Q}_n = 38.0$ kW; pathlines up to ≈ 1 s after ejection in room

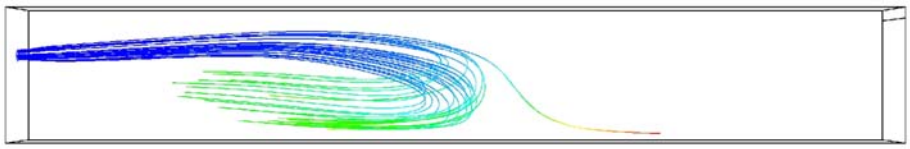

(b): methane, $D = 50$ mm, $\dot{Q}_n = 12.7$ kW; pathlines up to ≈ 3 s after ejection in room

Fig. 7 Pathlines from burner nozzle.

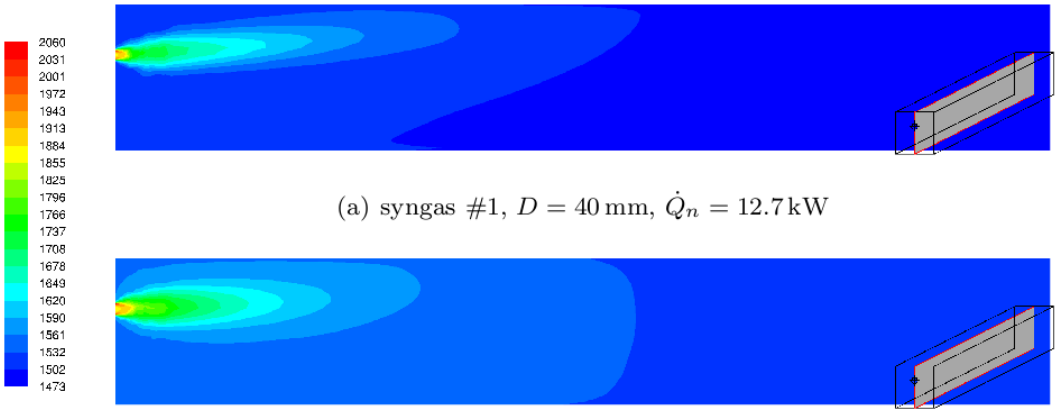

(a) syngas #1, $D = 40\,\text{mm}$, $\dot{Q}_n = 12.7\,\text{kW}$

(b) syngas #1, $D = 50\,\text{mm}$, $\dot{Q}_n = 12.7\,\text{kW}$

Fig. 8 Temperature field along kiln axial vertical plane (unit: K).

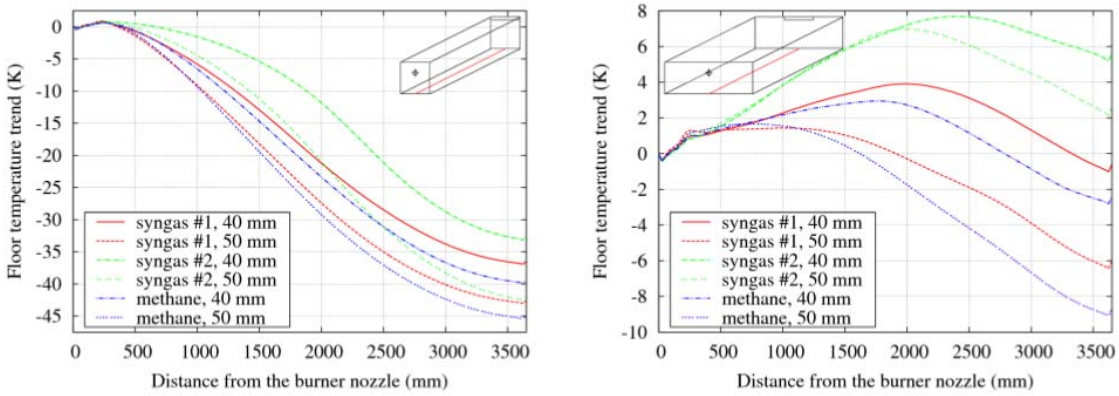

(a) $\dot{Q}_n = 12.7\,\text{kW}$ cases (b) $\dot{Q}_n = 38.0\,\text{kW}$ cases

Fig. 9 Axial temperature distribution on tiles floor (unit: K) and in terms of difference from floor temperature by nozzle location. Axial temperature distribution refers to the temperature distribution along the floor line placed vertically below the burner nozzle axis as shown in the outlines on the top of the figures.

clear how higher mass flow rates (that is to say, high $\dot{Q}_n$ cases) push the peak floor temperature up to 2500 mm away from the nozzle, while for lower mass flow rates the peak temperature distance never exceeds 300 mm. The temperature profile is quasi-parabolic, with the temperature rise in the first part of the floor slightly less steep than the descent on the far-end.

Aiming at the minimization of ΔT_{fl}, it is clear how the optimum solution should exhibit the same floor temperature at the extremities. From Fig. 9b it can be evinced that this is attainable when the floor peak temperature approximately falls 2000 mm away from the nozzle. This means that an optimum nozzle velocity, depending on the burner operating conditions, exists. Despite the fact that the simplified geometry, here adopted for computational reasons, is not fully representative of the actual functioning of a real kiln, this is a useful hint to the kiln designer. It must be reminded that in a real kiln, the fact that the burners are placed alternately on lateral walls would promote better temperature distributions than those foreseen here. Thus, the optimum temperature peak location will actually be nearer to the burner nozzle section, and the most critical kiln section is the central one. Typical values of ΔT_{fl} in industrial kilns are approximately the same as those predicted for high $\dot{Q}_n$ cases in the current study.

3.2 Low LHV fuels and energy balance

Thermal power enters the kiln room from the burner nozzle section in terms of hot air/fuel/exhaust gas mixture and can leave the system either from the walls in terms of heat loss, or from the outlet in terms of sensible enthalpy discharged with the exhaust gas. From an energy balance of the kiln module for the various operating conditions tested, it can be seen that the largest fraction of thermal energy, ranging from 57 % to 67 %, leaves the system through the outlet section. This fraction depends on the fuel type, but here does not depend on $\dot{Q}_n$ for the sole reason that the use of the three-fold burner power was adopted on a three-fold volume domain with a three-fold thermally active surface area.

This does not mean that in a real kiln such a large amount of thermal energy is wasted since industrial kilns are provided with energy recovery systems. However, it gives the idea of the thermal load that would fall on the heat exchangers of these recovery systems.

A few considerations on the impact that low LHV fuels have on the kiln behaviour are now in order. Low LHV fuels require larger fuel mass flow rates for a given thermal power. Despite the fact that low LHV fuels are also characterized by low air-to-fuel stoichiometric ratios, the total mass flow rate required is larger when compared to methane. Recalling Eqs. 3 and 4, and Table 2 the total mass flow rate per thermal power for the three fuels and for the given air excess is

$$\frac{\dot{M}_t}{\dot{Q}_n} = \frac{1.1\ AFS_{st} + 1}{LHV} = \begin{cases} 0.399\ \frac{\text{kg}}{\text{MJ}} & \text{for methane} \\ 0.450\ \frac{\text{kg}}{\text{MJ}} & \text{for syngas \#1} \\ 0.601\ \frac{\text{kg}}{\text{MJ}} & \text{for syngas \#2} \end{cases} \quad (6)$$

Since the average mixture atomic number does not differ much from case to case, low LHV fuels give larger velocities at the nozzle, that is to say better convection but also lower residence times. Considering the temperature uniformity over the tiles floor, slightly better results are expected, assuming the burner nozzles are properly tuned as discussed above, but at high costs in terms of energy. In fact, larger mass flow rates go along with larger sensible enthalpies at the chimney, which translates into higher costs for the heat recovery system and necessarily larger waste of energy.

Moreover, low LHV fuels also have low adiabatic flame temperature, and as the adiabatic flame temperature draws near to the room temperature needed for proper firing, the thermal power requirements grow exponentially.

This does not mean that the use of syngases for firing tiles in industrial kilns must be discouraged; on the contrary it can be an opportunity. It is true, however, that a complete and not necessarily straightforward re-calibration of the firing process is needed.

4. CONCLUSIONS

CFD analyses of a module of an industrial kiln for ceramic tiles production have been performed. The study aimed at assessing the behaviour of the kiln in terms of temperature and velocity distributions in the heated room, and in terms of temperature uniformity on the tiles floor in case the kiln is operated using different synthesis gases in place of methane.

It is noted that the use of different fuels, having different LHVs, implies rather different gas mass flow rates into the system, which affect convection, and thus the temperature distribution. Similar consequence applies to the use of different nozzle diameters, or burner nominal powers. By manipulating these parameters, it is

possible to promote a more uniform temperature distribution over the tiles floor.

Since there is no need of firing under dynamic temperature conditions, active control of the firing parameters is rarely adopted in industrial kilns for tiles production, thus the burners are commonly operating under steady-state conditions. Higher burner nominal power will be used in those sections of the kiln where the lengthwise temperature profile is supposed to rise quickly, while lower power will be used where the temperature should be kept constant or should decrease. Moreover, it is very unlikely that different types of fuel are used on a single kiln since this would entail unaffordable complications to the fuel supply piping system.

Thus, the only option that remains for controlling the spanwise temperature distribution is given by the burner nozzle shape and diameter. Of course, the best choice would be to adopt different diameters for each burner depending on its standard operating conditions, but this would be neither practical nor cost effective. Nevertheless, in view of optimizing the kiln performance, it could be viable to adopt just a few different burner nozzle diameters to be used with different burners: e.g. differentiating between those working at high or low nominal power.

In future work it would be of interest to address the simulation of a wider section of the kiln in order to be able to account for the effects of the lengthwise flow along the kiln room. In any case, the mesh generation and the CFD analysis set-up should be addressed carefully since the computational cost may increase radically.

NOTATION

AFR_{st}	Stoichiometric air-to-fuel ratio
D	Burner nozzle diameter
k	Turbulent kinetic energy
LHV	Fuel gas lower heating value
$\dot{M}_a$	Air mass flow rate
$\dot{M}_f$	Fuel gas mass flow rate
$\dot{M}_t$	Total mass flow rate
$\dot{Q}_n$	Nominal burner power
f_m	Mean mixture fraction
f_v	Mean mixture fraction variance
S	Sutherland temperature
T	Mixture temperature
T_0	Reference temperature
T_{fl}	Average temperature on tiles floor
T_{rm}	Average temperature in kiln room
$\boldsymbol{v}$	Velocity
ΔT_{fl}	Maximum temperature difference on tiles floor
ε	Turbulent dissipation rate
μ	Mixture dynamic viscosity
μ_0	Reference dynamic viscosity
μ_t	Turbulent dynamic viscosity
ρ	Density

REFERENCES

1. Boulet M, Marcos B, Dostie M, Moresoli C (2010). CFD modeling of heat transfer and flow field in a bakery pilot oven. *Journal of Food Engineering* 97:393-402.
2. Cavazzuti M, Corticelli MA, Nuccio A, Zauli B (2013). CFD analysis of a syngas-fired burner for ceramic industrial roller kiln. *Proceedings of the Institution of Mechanical Engineers, Part C: Journal of Mechanical Engineering Science* 227: 2600-2609.
3. Mastorakos E, Massias A, Tsakiroglou CD, Goussis DA, Burganos VN, Payatakes AC (1999). CFD predictions for cement kilns including flame modelling, heat transfer and clinker chemistry. *Applied Mathematical Modelling* 23:55-76.
4. Mikulčić H, Vujanović M, Fidaros DK, Priesching P, Minić I, Tatschl R, Duić N, Stefanović G (2012). The application of CFD modelling to support the reduction of CO_2 emissions in cement industry. *Energy* 45:464-473.
5. Mirade PS, Daudin JD, Ducept F, Trystram G, Clément J (2004). Characterization and CFD modelling of air temperature and velocity profiles in an industrial biscuit baking tunnel oven. *Food Research International* 37:1031-1039.
6. Smolka J, Nowak AJ, Rybarz D (2010). Improved 3-D temperature uniformity in a laboratory drying oven based on experimentally validated CFD computations. *Journal of Food Engineering* 97:373-383.
7. Söğüt Z, Oktay Z, Karakoç H (2010). Mathematical modeling of heat recovery from a rotary kiln. *Applied Thermal Engineering* 30:817-825.
8. Therdthai N, Zhou W, Adamczak T (2004). Three-dimensional CFD modelling and

simulation of the temperature profiles and airflow patterns during a continuous industrial baking process. *Journal of Food Engineering* 65:599-608.

9. Williamson ME, Wilson DI (2009). Development of an improved heating system for industrial tunnel baking ovens. *Journal of Food Engineering* 91:64-71.
10. Wong SY, Zhou W, Hua J (2006). Robustness analysis of a CFD model to the uncertainties in its physical properties for a bread baking process. *Journal of Food Engineering* 77:784-791.